frontiers | Frontiers in Mechanical Engineering

TYPE Original Research
PUBLISHED 03 February 2026
DOI 10.3389/fmech.2025.1743715

OPEN ACCESS

EDITED BY
Evangelos G. Giakoumis,
National Technical University of Athens, Greece

REVIEWED BY
Satyam Panchal,
University of Waterloo, Canada
Anirban Sur,
Symbiosis International University, India

*CORRESPONDENCE
Duc Trong Nguyen,
2022603200@st.haui.edu.vn,
nguynductrong16@gmail.com

RECEIVED 11 November 2025
REVISED 11 December 2025
ACCEPTED 24 December 2025
PUBLISHED 03 February 2026

CITATION
Pham M, Chan T-C, Chu DH, Ngo HT, Do VT, Dinh NA, Pham HA and Nguyen DT (2026) CFD analysis of directional airflow and internal baffles for improving thermal uniformity in a 4 × 6 li-ion battery module.
Front. Mech. Eng. 11:1743715.
doi: 10.3389/fmech.2025.1743715

CFD analysis of directional airflow and internal baffles for improving thermal uniformity in a 4 × 6 li-ion battery module

Minhhieu Pham[1], Tzi-Chi Chan[2], Duc Hung Chu[1], Huu Tinh Ngo[1], Van Tuan Do[2], Ngoc Anh Dinh[1], Hong An Pham[1] and Duc Trong Nguyen[1]*

[1]School of Mechanical and Automotive Engineering, Hanoi University of Industry, Hanoi, Vietnam, [2]Department of Mechanical and Computer-Aided Engineering, National Formosa University, Huwei, Taiwan

Effective thermal management for lithium-ion batteries is a key factor in preventing overheating, maintaining even heat distribution, and extending battery life. Air cooling systems are considered a simple, low-cost, and easy-to-implement solution. However, poor heat transfer efficiency and uneven airflow remain major challenges. This study investigates the impact of airflow direction and internal partitions on the thermal performance of a 4 × 6-cell lithium-ion battery module using Computational Fluid Dynamics (CFD) simulations with ANSYS Fluent software. Five cooling configurations were investigated. The results showed that the novel combination of counter-flow air with internal partitions provided the most optimal cooling performance. This synergy significantly enhanced thermal uniformity and helped maintain safer operating temperatures. Specifically, the maximum temperature T_{max} decreased from 346.852 K to 314.768 K, and the temperature difference between cells ΔT_{max} decreased sharply from 39.7 K to only 2.9 K. The partition enhanced convection and effectively prevented airflow from short-circuiting. Nevertheless, this design also increased pressure loss and fan power consumption by approximately 10%-12% compared to the base configuration. Simulation results demonstrated the superior effectiveness of the combined counterflow and baffle design in air cooling solutions, while providing a technical basis for optimizing a low-cost, high-efficiency, and easily deployable Battery Thermal Management System (BTMS) in practice.

KEYWORDS

air cooling, battery thermal management, CFD simulation, internal baffle, pressure drop

1 Introduction

Lithium-ion batteries are currently the leading energy storage technology, widely used in electric vehicles, electronic devices, and renewable energy storage applications due to their high energy density, excellent stability, and efficient charging/discharging capabilities (Chen et al., 2020; Aghajan-Eshkevari et al., 2022; Zhu et al., 2020). On the other hand, battery operation generates heat, especially during high-current discharge or fast charging, which can lead to overheating (Qian et al., 2023). When the battery temperature surpasses 60 °C–70 °C, performance is significantly compromised and lifespan is shortened. More critically, elevated temperatures pose a serious risk of thermal runaway-defined as a chain of

TABLE 1 Specifications of Panasonic 18650 LIB batteries.

Length (mm)	Diameter (mm)	Minimum voltage (V)	Normal voltage (V)	Maximum voltage (V)	Capacity (mA.h)
65	18	2.5	3.6	4.2	3,000

uncontrollable thermochemical reactions that can result in fire and explosion (Feng et al., 2020; Li et al., 2022). For this reason, effective temperature control, especially in dense battery module configurations like electric vehicles, has become one of the most critical challenges in designing the BTMS (Murugan et al., 2025; Pham et al., 2025).

Among the thermal management solutions currently under consideration, forced air cooling is a simple, low-cost option that does not suffer from leakage issues, is easy to integrate and maintain, and is particularly suitable for light electrical applications or small electric vehicles (Lin et al., 2021). In contrast, low heat transfer coefficients and uneven heat distribution are significant limitations of air-cooling systems, especially when battery cell density is high and airflow space is limited (Chen et al., 2024; Al-Zareer et al., 2018). Consequently, optimizing the configuration of battery cell layout and airflow design within the battery module has become a primary focus in many recent studies.

Recent studies have focused on clarifying the impact of geometric factors and airflow direction on the heat transfer performance of air-cooled lithium-ion battery modules (Satheesh et al., 2021; Li et al., 2024). The study by Wang et al. demonstrates that altering the distance between cells can enhance thermal uniformity, however, if the distance exceeds the optimal limit, it increases the module volume and decreases heat exchange efficiency (Zhao et al., 2021). Meanwhile, Satheesh et al. (2021) demonstrated that adjusting the cross-section of the air duct to a conical shape increases airflow velocity and improves local heat dissipation without increasing fan flow rate. Lin et al. (2024) indicated that the use of honeycomb flow guides distributed the airflow evenly, significantly reducing the temperature difference between cells to below 5 °C–the limit considered a safety standard in BTMS design. Additionally, Argade and De (2024) proposed a z-flow airflow arrangement combined with auxiliary exhaust ports, which improved the maximum temperature difference by 72.84% compared to a cooling model without auxiliary exhaust ports. More recently, advanced passive solutions, such as phase change materials (PCM) integrated with fins, are explored to overcome air cooling limitations by enhancing thermal capacity and heat transfer (Narkhede et al., 2025). The development trend suggests combining optimized flow geometry with novel materials, like polymer heat sinks or internal baffles, to achieve necessary thermal uniformity without incurring prohibitive energy penalties (Sur et al., 2023). Building on these concepts, high-performance BTMS increasingly rely on complex hybrid solutions, such as nano-PCM integrated with minichannels or optimized indirect liquid cooling, to attain superior thermal uniformity, yet these strategies inherently increase manufacturing cost and complexity (Hmidi et al., 2026; Mohapatra et al., 2025; Sarvestani et al., 2025). However, most of these studies focus only on the overall layout of the module or adjusting the air flow, while paying little attention to the impact of internal partitions within the module, which can significantly alter the air flow (Satheesh et al., 2021; Zhang et al., 2023). In practice, compartmentalization using partitions is a solution applied to direct airflow to specific areas while preventing short-circuit flow, but there is still a lack of a clear scientific basis for quantifying the effectiveness of this design.

The paper developed a thermal simulation model on a 6 × 4 lithium-ion battery module configuration with different layouts and with/without internal partitions (Madani et al., 2025; Xie et al., 2025), while also combining changes in the direction of the cooling airflow entering the battery module in cases with more than one inlet/outlet (Li et al., 2024; Oyewola et al., 2024). The objective was to evaluate the impact of partitions, vent hole arrangements, and cooling airflow direction on key thermal parameters such as maximum temperature, thermal uniformity, and thermal field distribution (Oyewola et al., 2024; Na et al., 2018). Using flow and heat transfer simulation methods combined with ANSYS Fluent simulation software, the study provides a quantitative view of the cooling efficiency of each configuration, thereby providing practical design recommendations for air-based BTMS solutions (Makings et al., 2024; Bamrah et al., 2022). The research results can serve as a technical foundation for optimizing battery packs with high requirements for cost, durability and safety (Khan et al., 2025).

2 Methodology

2.1 Geometric model design

The commercial Panasonic 18650 LIB battery was selected for this study (Muenzel et al., 2015). Detailed specifications of the battery, including its length, diameter, and capacity, are presented in Table 1:

The forced air cooling battery module model used consists of 24 4 × 6 battery cells enclosed by an outer casing (Bamrah et al., 2022; Zhang et al., 2020), as shown in Figure 1. The position of the ventilation holes used in this study is intentionally placed between the battery cells, rather than in the traditional center of the A/C face as seen in the research by Ko et al. (2021), to directly increase the contact area between the cells and the cool airflow. This design choice is critical for enhancing local convective heat transfer, preventing short-circuiting flow, and effectively directing the hot airflow out of the module (Mustafa, 2022; Jin et al., 2021; Zhao et al., 2023). The battery cell model used in this study consists of a solid cylinder considered as the battery cell core, with a diameter of 18 mm and a height of 65 mm, and a hollow cylinder considered as the battery cell shell with an inner diameter of 18 mm, an outer diameter of 19 mm, and the same height. The module utilizes a compact 4 × 6 cell configuration with 20 mm axial spacing to maximize energy density. However, this geometry inherently creates narrow channels that restrict airflow, causing flow blockage and substantial thermal gradients, resulting in localized hot spots in the central region. This constitutes the critical thermal challenge that the study aims to mitigate through optimized airflow and internal partitions

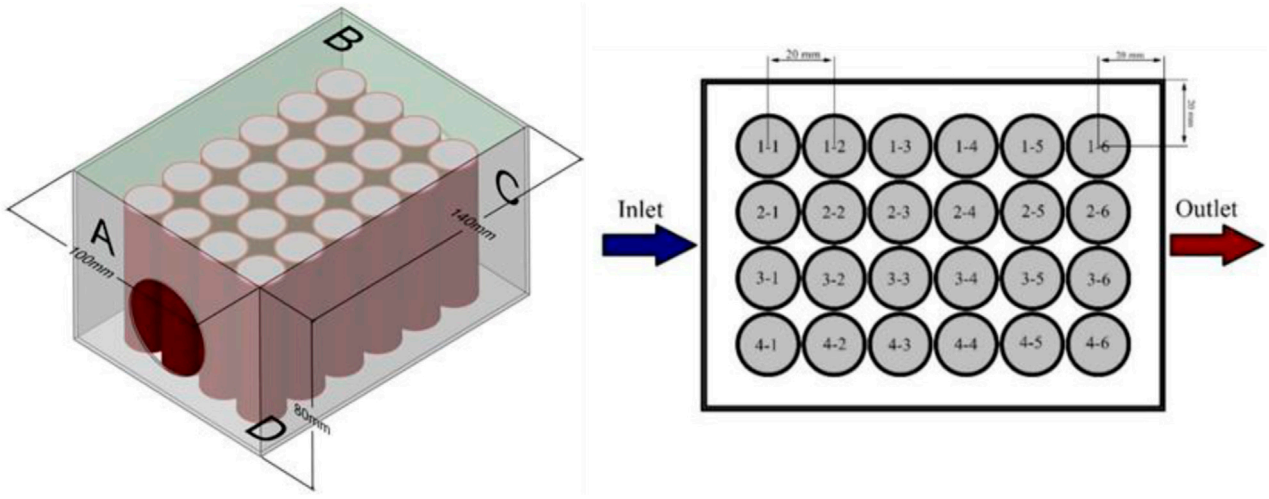

FIGURE 1
Lithium battery module model with 4 × 6 cells.

(Murphy and Akrami, 2024; Peng et al., 2020; Masthan Vali et al., 2025). Each cell is labeled in a row-column format, and the battery cells are numbered sequentially from left to right along with the direction of the cooling air flow (Murphy and Akrami, 2024). The heat generated by the battery cells is transferred through the cooling airflow entering from the inlet, then exits via the forced airflow. The calculations and simulations presented in this study were performed using Ansys Fluent software (Masthan Vali et al., 2025; Nicholls, 2024).

This study investigates and evaluates the changes in the number of inlets and outlets, with and without partitions parallel to the bottom, and the direction of airflow on the cooling performance of the battery module (Mustafa, 2022; Zhao et al., 2023). Changes in the cooling system design must ensure that the airflow into the battery module remains constant in all cases. To facilitate the evaluation of cooling performance for each case, the diameter of the inlets and outlets in the single inlet/outlet case is 40 mm for one hole and 28 mm for one hole in the dual inlet/outlet case, as shown in Figure 2.

In optimal cases, aluminum directional partitions have been integrated to address the issue of uneven heat distribution. These 1 mm-thick partitions are arranged along the module and placed at the midpoint of the cell height (Oyewola et al., 2024; Na et al., 2018; Zhang et al., 2022). Illustrated in Figure 3.

The primary function of the partition is to force the cooling airflow through narrow gaps between the cells, thereby effectively preventing short-circuiting and enhancing the uniformity of convective heat transfer (Zhang et al., 2023; Oyewola et al., 2024; Zhang et al., 2022). Table 2 summarizes the five flow configurations and geometries investigated in this study.

2.2 Foundation equation

2.2.1 The amount of heat generated from the battery

In this study, Bernardi's thermal model (Elmahallawy et al., 2022) was selected due to its simplicity, allowing direct representation of the relationship between thermal variables while ensuring the necessary accuracy. The heat generated in the battery cells during operation is represented by the following energy balance equation:

$$\dot{Q} = Qjoule + Qentropy = (v - v_{OCV})I + IT\frac{dV_{OCV}}{dT}$$

Where: Q is the heat generated, v is the cell voltage, v_{ocv} is the open-circuit voltage, I is the current intensity, and T is the cell temperature.

This study examines all simulation cases at a discharge current of 3C. (The C-rate is defined as the measure of the charge or discharge current relative to the nominal capacity of the battery, where 1C means the battery is fully charged or discharged in 1 h). The heat generation coefficient per unit volume in the LIB battery is taken as a constant 48,750 W/m^3 and is assumed to be uniform across the entire battery cell volume based on the formula for heat generation, which is expressed as follows:

$$Q_t = R.I^2$$

Where: Q_t is the heat generation coefficient per unit volume, R is the internal resistance in the lithium battery cell, and I is the current intensity. In this study, R = 10 mΩ is used in all cases.

2.2.2 Equations governing gases

To determine the appropriate flow model for the fluid in the study, the Reynolds number is calculated to classify the flow regime of the cooling air as laminar flow, turbulent flow, or transitional flow. The Reynolds number is determined using the formula:

$$R_e = \frac{\rho.v.D}{\mu}$$

Where: R_e is the Reynolds number, ρ is the density of air, v is the velocity of the air flow, D is the cross-sectional area of the inlet, and μ is the dynamic viscosity of air.

Since the Reynolds numbers are determined to be greater than 2,300 for the single inlet and dual inlet cases, respectively, turbulent

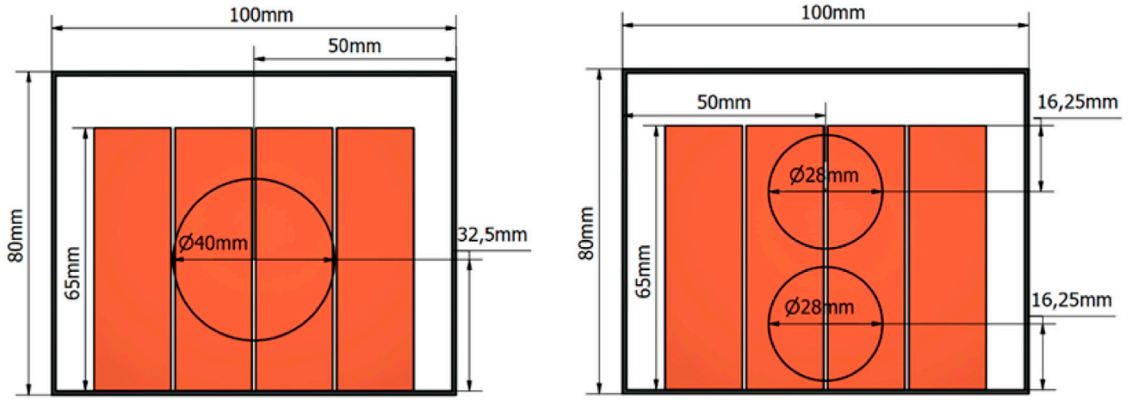

FIGURE 2
Ventilation hole location of the module.

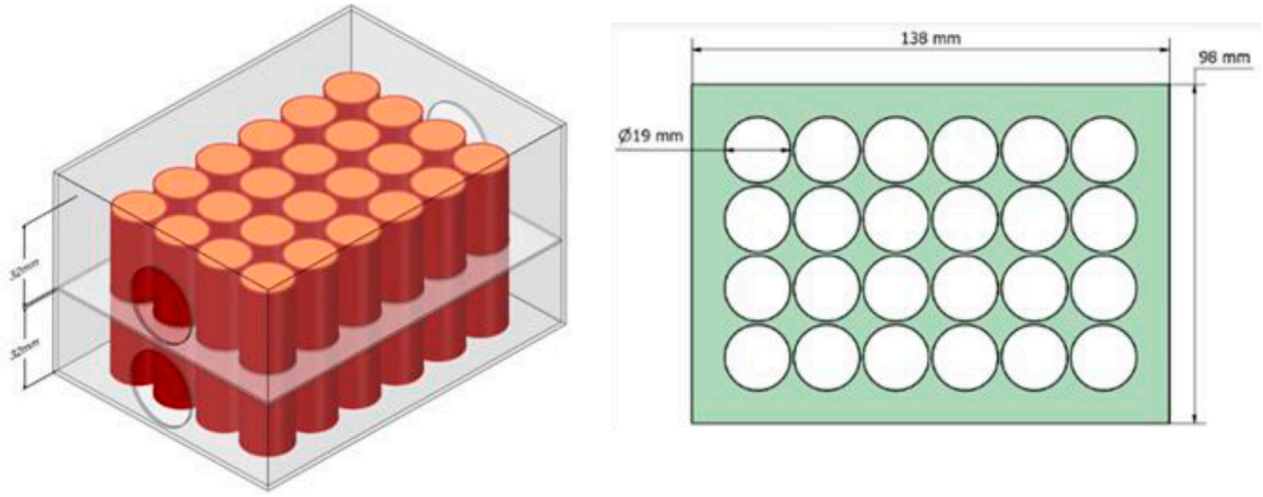

FIGURE 3
Design of the partitioned middle battery cells.

flow regimes, including laminar flow, turbulent flow, and transitional flow are employed for the air-cooled lithium battery cooling system. The governing equations for the flow are presented as follows (ANSYS and Inc, 2025):

Continuity equation:

$$\frac{\partial \rho}{\partial t} + \nabla . \rho \overrightarrow{v_r} = 0$$

Momentum conservation equation:

$$\frac{\partial}{\partial t}\rho\vec{v} + \nabla \cdot \left(\rho\vec{v}_r\vec{v}\right) + \rho[\vec{\omega}.(\vec{v}-\vec{v}_t)] = -\nabla p + \nabla \cdot \bar{\bar{\tau}} + \vec{F}$$

And the energy conservation equation:

$$\frac{\partial}{\partial t}\rho E + \nabla \cdot \left(\rho\vec{v}_r H + p\vec{u}_r\right) = \nabla \cdot \left(k\nabla T + \bar{\bar{\tau}} \cdot \vec{v}\right) + S_h$$

In this context, ρ is the density of the fluid, $\vec{v}$ is the absolute velocity, $\vec{v}_r = \vec{v} - \vec{v}_f$ is the relative velocity between the flow and the moving frame, where $\vec{v}_f$ is the velocity of the computational domain. The quantities $\vec{v}_t$ and $\vec{\omega}$ are the translational and angular velocities of the reference frame, respectively. p is the static pressure, τ is the viscous stress tensor, and $\vec{F}$ is the volumetric force, typically gravity. In the energy equation, E is the total energy per unit mass, $H = E + \frac{p}{\rho}$ is the total enthalpy, k is the thermal conductivity coefficient, T is the absolute temperature, and S_h is the volumetric heat source. The symbols ∇ and $\nabla\cdot$ represent the gradient and divergence operators in space, respectively.

The characteristics of turbulent flow are simulated in Ansys Fluent software using a turbulence model. k-ε standard, the turbulence kinetic energy-k, and its rate of dissipation-ε, are

TABLE 2 Survey cases.

Case	Description
1	1 inlet 1 outlet, no partition
2	2 inlets 2 outlets, 2 air streams in the same direction, no partition
3	2 inlets 2 outlets, 2 air streams in opposite directions, no partition
4	2 inlets 2 outlets, 2 air streams in the same direction, with a partition
5	2 inlets 2 outlets, 2 air streams in opposite directions, with a partition

obtained from the following transport equations (ANSYS and Inc, 2025):

$$\frac{\partial}{\partial t}(\rho k) + \frac{\partial}{\partial x_i}(\rho k u_i) = \frac{\partial}{\partial x_j}\left[\left(\mu + \frac{\mu_t}{\sigma_k}\right)\frac{\partial k}{\partial x_j}\right] + G_k + G_b - \rho\varepsilon - Y_M + S_k$$

And

$$\frac{\partial}{\partial t}(\rho\varepsilon) + \frac{\partial}{\partial x_i}(\rho\varepsilon u_i) = \frac{\partial}{\partial x_j}\left[\left(\mu + \frac{\mu_t}{\sigma_\varepsilon}\right)\frac{\partial \varepsilon}{\partial x_j}\right] + C_{1\varepsilon}\frac{\varepsilon}{k}(G_k + C_{3\varepsilon}G_b) - C_{2\varepsilon}\rho\frac{\varepsilon^2}{k} + S_\varepsilon$$

Where k is the kinetic energy of turbulence representing the intensity of velocity fluctuations, and ε is the dissipation rate of turbulent energy. ρ is the fluid density, μ is the dynamic viscosity, and $\mu_t = \rho C_\mu \frac{k^2}{\varepsilon}$ is the turbulent viscosity, where $C_\mu = 0.09$. The empirical constants of the model include $C_{1\varepsilon} = 1.44$, $C_{2\varepsilon} = 1.92$, $\sigma_k = 1.0$ and $\sigma_\varepsilon = 1.3$. G_k and G_b respectively represent the turbulent energy generated by the velocity gradient and buoyancy force. These equations are solved simultaneously with the RANS system to describe the formation, development, and dissipation of turbulence in the flow.

2.2.3 Evaluation parameters

To evaluate the energy consumption of the cooling system, the fan power required to overcome the pressure loss (ΔP) across the pin module is determined based on the average pressure difference between the inlet and outlet cross-sections. In this study, assuming that a single fan is used to supply air to all inlets in the module, the required fan power (P) is determined by the formula (Mustafa, 2022; Zhao et al., 2023):

$$\mathrm{P} = \frac{(\Delta P \,.\, Q)}{\eta}$$

With Q being the total cooling air flow volume of 1.25×10^{-3} m^3/s, kept constant in all cases to ensure fair comparison, and η being the fan efficiency, assumed to be 0.6, a realistic value for industrial centrifugal fans.

To quantify the improvement level of each cooling configuration compared to the baseline configuration, the study uses the normalized reduction ratio (NRR) metric (Satheesh et al., 2021; Murphy and Akrami, 2024). This metric allows quantitative comparison between configurations for characteristic parameters such as maximum temperature T_{max}, maximum temperature difference ΔT_{max} and fan power P. NNR is calculated using the formula:

$$\mathrm{NRR} = \frac{(X_{Casi\,1} - X_{Case\,i})}{X_{Case\,1}}\,100\%$$

In which $X_{Case\ 1}$ is the reference value of the indicator (T_{max}, ΔT_{max}, or P) in the base configuration, while $X_{Case\ i}$ is the corresponding value in the configuration under consideration. A positive NRR value indicates an improvement (reduction in maximum temperature, reduction in temperature difference, or reduction in fan power), while a negative NRR indicates a decrease in performance or an increase in energy consumption compared to the baseline.

2.3 Boundary conditions and numerical modeling

2.3.1 Boundary conditions

This study examines the stable inlet cooling air velocity at 1 m/s, corresponding to a total flow rate of 1.25×10^{-3} m^3/s for the case with one inlet/outlet. As described in Section 2.1, the total cooling air flow rate entering the battery module is maintained as constant in all cases studied to ensure a fair comparative basis solely dependent on geometric configuration. Therefore, when the number of inlets increases, the air flow rate is divided equally among each inlet. Maintaining a constant total cooling airflow across all configurations is crucial. This ensures a fair comparison of the thermal performance improvements achieved solely by changes in module geometry and flow direction. The inlet temperature of the cooling air stream is set equal to the ambient temperature of 25 °C, and the pressure is equal to atmospheric pressure. The settings for the velocity, temperature, and pressure of the cooling air stream have been selected. Next, the conditions at the module shell are set to be non-slip and with zero relative pressure at the outlet. Thermal boundary conditions are applied to the surfaces of the battery module because the space for installing the battery module is often small and confined. Furthermore, The effect of thermal radiation emitted by the battery surfaces is not considered in this study. This simplification reduces computational complexity and ensures that heat transfer analysis is governed primarily by forced convection and conduction within the module, focusing the simulation on the dominant cooling mechanism.

The material used for the core of the battery cell is Lithium, while all other components are made of Aluminum, including the module casing, battery cell casing, and separator. The characteristics of the materials are presented in Table 3:

The simulations were performed using Ansys Fluent software based on the steady flow-heat transfer model. The Standard k-ε turbulence model combined with Enhanced Wall Treatment was used to accurately describe the boundary layer region and turbulent flow characteristics in the narrow channels of the pin module. This model was selected for its proven balance between accuracy and computational efficiency in internal flow problems, while the Enhanced Wall Treatment is crucial for resolving the velocity and temperature gradients within the near-wall region of the narrow gaps between the cells. The energy equation was activated for both the solid and gas phases to simultaneously simulate the heat transfer and convection processes.

TABLE 3 Material properties.

Material	c (J.kg^{-1}.k^{-1})	ρ (kg.m^{-3})	k (W.m^{-1}.k^{-1})	μ (Pa.s)
Lithium	1,200	2,500	4	-
Aluminum	871	2,719	202.4	-
Cooling air	1,005	1,204	0.0267	1.5×10^{-5}

TABLE 4 Grid independence.

Level	Cells	T_{max} (K)	Relative error between the current and previous mesh (%)
Mesh 1 (coarse)	647,842	347.388	-
Mesh 2 (medium – coarse)	971,764	347.091	0.0855
Mesh 3 (baseline/medium)	1,295,683	346.852	0.0689
Mesh 4 (medium – fine)	1,943,525	346.798	0.0156
Mesh 5 (fine)	3,887,049	346.761	0.0107

Second-order discretization algorithms were selected for the velocity, temperature, and turbulence variables. The time step was set to $\Delta t = 0.5$ s, ensuring numerical stability and the ability to capture the initial heat transfer process. The convergence criterion was set at $<10^{-6}$ for velocity and pressure, and $<10^{-7}$ for energy. Simulations are run until the quantities meet the convergence criteria, T_{max} and ΔT_{max} change less than 1% over 10 consecutive seconds, which is considered a stable state. The module casing is treated as adiabatic walls, assuming negligible heat exchange with the ambient environment due to the typical insulated packaging of battery packs, and all gas-solid surfaces are set to no-slip conditions. Results are output every 0.1 s to facilitate analysis of thermal evolution over time.

2.3.2 Independent grid assessment

The computational domain was discretized using ANSYS Meshing. We employed a non-conformal mesh, utilizing polyhedral elements for the fluid domain and structured hexahedral elements for the solid cell cores and casing. Specific sizing controls were applied to refine the mesh, particularly in the narrow gaps between the cylindrical cells and near the internal partitions, where high velocity and temperature gradients are expected. The meshing strategy was designed to maintain high mesh quality (maximum skewness below 0.85), ensuring numerical stability. This setup, combined with our boundary layer treatment, guarantees accurate modeling of momentum and heat transfer in the critical near-wall regions.

To ensure the independence of simulation results from computational grid resolution, we conducted a detailed grid independence study on the base model with 1 inlet and 1 outlet (Case 1) by comparing the maximum temperature at 5 different grid densities. The grid was constructed using an incremental method to increase the number of elements, with 1,295,683 elements identified as the base grid for the official simulations of this study. Five mesh levels were created, ranging from the coarsest level with 647,842 elements to the finest level with 3,887,049 elements. The T_{max} values recorded after the simulation reached a steady state are presented in Table 4.

The analysis clearly shows the process of numerical convergence, as the grid resolution increases from Mesh 1 to Mesh 3, the T_{max} value decreases significantly. This change, with relative differences of 0.0855% and 0.0689% between adjacent grid pairs, reflects that the velocity and temperature fields have been modeled in greater detail. Continuing to refine the grid to Meshes 4 and 5 levels, the change in T_{max} becomes minimal. The absolute difference between Mesh 4 and Mesh 5 is only 0.037 K.

The relative difference between the two finest mesh levels (Mesh 4 and Mesh 5) was determined to be 0.0107%. This value is significantly lower than the standard acceptance threshold in CFD (≤1%). This convergence demonstrates that mesh independence has been successfully established. For this reason, a mesh with 1,295,683 elements was selected to perform all remaining simulations, as the relative difference in T_{max} compared to the finest mesh is only 0.091 K. This choice ensures high accuracy for the physical results, while optimizing the computational cost and time for the entire study.

3 Results and discussion

The objective of this study is to design a cooling system for a 4 × 6 Lithium battery module to minimize the temperature of the battery cells and maintain a temperature difference between the cells of no more than 5 K. These parameters will be presented and addressed using CFD simulation software-Ansys Fluent. First, the study will present the results of the basic configuration cooling model, without partitions.

3.1 Cooling performance of the basic configuration model–without partitions

3.1.1 1 inlet – 1 outlet model

In this study, the 1 inlet – 1 outlet configuration was selected as the base model to provide a reference platform for subsequent

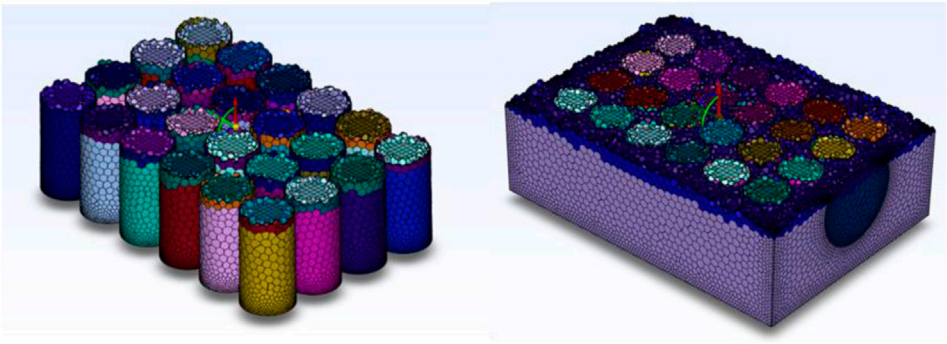

FIGURE 4
Computational model meshing.

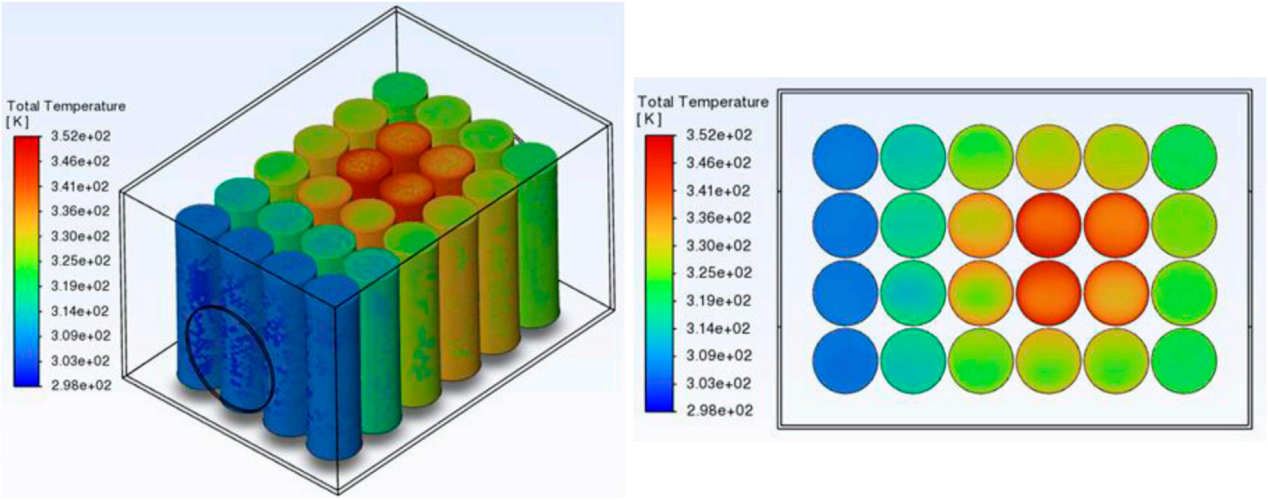

FIGURE 5
Temperature distribution in the 1 inlet – 1 outlet model.

analyses. This model is derived from the research of Zhang et al. (2020). However, the cooling efficiency of this configuration has many limitations, especially in the center of the battery module with uneven heat distribution and maximum temperatures exceeding the recommended threshold. Therefore, using the base model ensures scientific continuity while providing a clear basis for comparison with improvement options regarding inlet/outlet arrangement, partition addition, or flow direction solutions in the current study.

The simulation results of the base configuration in this study show a heat distribution trend similar to previous studies, where cells near the inlet are cooled more effectively while the center and downstream areas of the battery module experience significant heat accumulation.

In this basic configuration with one inlet and one outlet, the simulation shows that the temperature distribution in the 4 × 6 cell module is highly uneven. The maximum temperature reaches approximately 346.852 K at the central cells (2-4, 3-4, 2-5, 3-5), while the minimum temperature of approximately 307.099 K occurs at the cells near the inlet (1-1, 2-1, 3-1, 4-1). On the other hand, the battery cells in the last row near the exit were cooled better than the central battery cells, as shown in Figures 4, 5.

The reason is that the cells in the central region are affected by the flow blockage phenomenon, causing a significant reduction in air velocity and poor convective heat transfer, leading to high temperature accumulation as illustrated in Figure 6. Conversely, the cells in the rear row near the outlet are affected by the suction effect, where the airflow is accelerated towards the outlet and reaches a higher velocity. As a result, the convective heat transfer coefficient is enhanced here, causing the rear row cells to have lower temperatures than the cells in the central region. The average temperature parameters for each cell are presented in Table 5.

The maximum temperature difference of approximately 39.7 K between battery cells 2-1 (minimum) and 2-4 (maximum) far exceeds the recommended threshold of 5 K, reflecting a fundamental drawback of this configuration: cells near the inlet

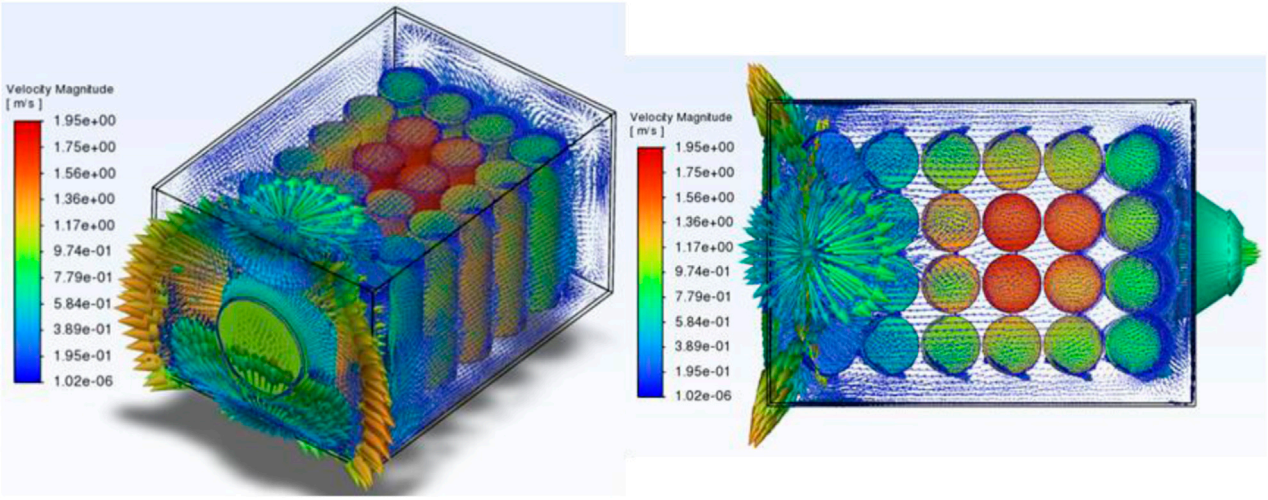

FIGURE 6
Distribution of cooling airflow in the module.

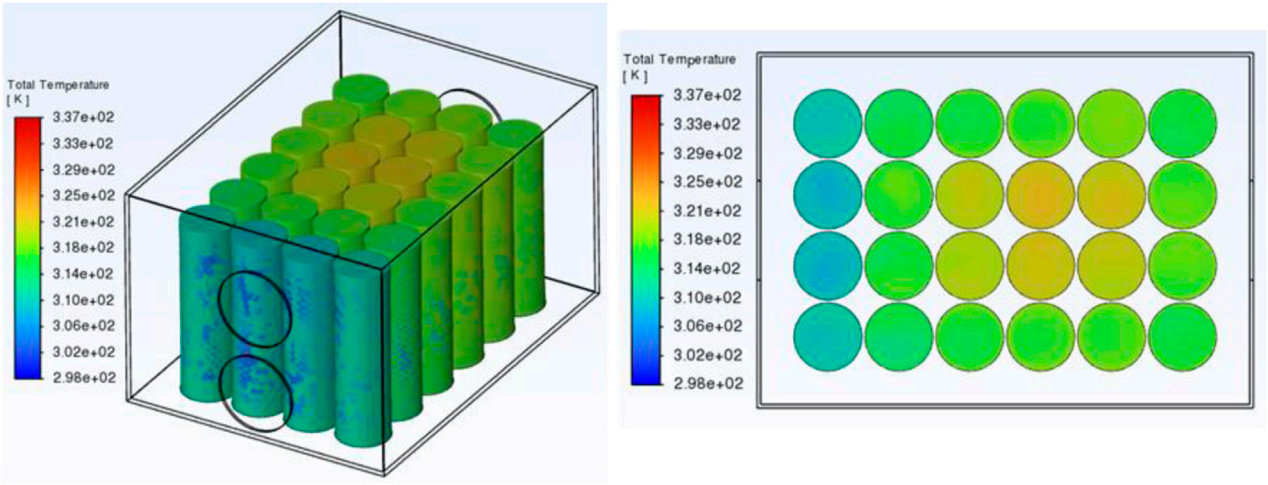

FIGURE 7
Temperature distribution in the 2 inlets-2 outlets module, with the same-direction airflow.

TABLE 5 Average temperature of each battery cell.

Cell	T (K)	Cell	T (K)	Cell	T (K)	Cell	T (K)
1-1	307.342	2-1	307.099	3-1	307.179	4-1	307.347
1-2	317.765	2-2	319.490	3-2	319.572	4-2	317.795
1-3	328.327	2-3	337.306	3-3	337.721	4-3	328.072
1-4	333.249	2-4	346.852	3-4	346.584	4-4	333.117
1-5	332.386	2-5	344.313	3-5	344.646	4-5	332.043
1-6	324.795	2-6	329.754	3-6	329.091	4-6	324.577

TABLE 6 Average temperature of each battery cell.

Cell	T (K)	Cell	T (K)	Cell	T (K)	Cell	T (K)
1-1	311.489	2-1	310.923	3-1	310.893	4-1	311.447
1-2	315.027	2-2	315.921	3-2	315.889	4-2	314.978
1-3	317.207	2-3	319.213	3-3	319.194	4-3	317.173
1-4	318.462	2-4	320.715	3-4	320.701	4-4	318.438
1-5	318.675	2-5	320.702	3-5	320.686	4-5	318.698
1-6	317.502	2-6	318.755	3-6	318.755	4-6	317.519

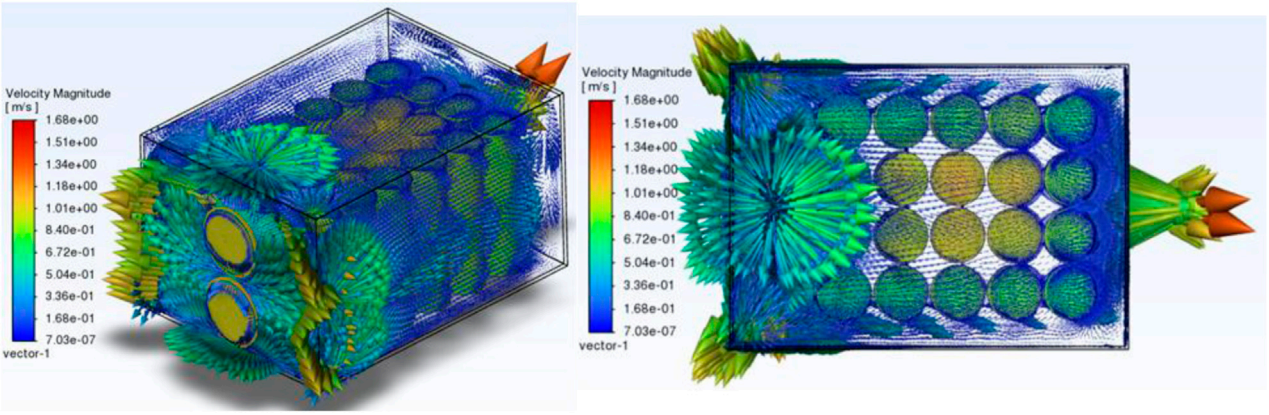

FIGURE 8
Distribution of cooling airflow in the module with 2 inlets and 2 outlets.

are well-cooled, while the central and downstream areas accumulate heat, forming hot spots. Although it does not yet meet practical thermal management requirements, this baseline model remains an important reference foundation for subsequent comparative analysis and design optimization.

3.1.2 2 inlets-2 outlets model, airflow entering in the same direction

With this test model, we arranged two inlets between the battery blocks, with each inlet responsible for cooling one half of the battery cells. The two cooling air streams entering the module flow in the same direction. Simulation results show that the cooling efficiency of the battery module is significantly improved compared to the base model. The airflow distributed from the two inlets enhances forced convection and minimizes heat accumulation in the central region. The maximum temperature in the module reached approximately 320.715 K at cells 2-4, which is significantly lower than the 346.852 K in the 1 inlet-1 outlet case, while the minimum temperature remained at approximately 310.893 K at the cells near the inlet. As a result, the maximum temperature difference between battery cells throughout the entire module is reduced to approximately 9.9 K, compared to 39.7 K in the base configuration as shown in Figure 7. This more uniform heat distribution reflects the important role of multi-inlet/outlet arrangement in reducing hot spots in the central area, thereby improving the safety and operational reliability of the battery system. To further clarify the thermal distribution efficiency in the 2 inlets-2 outlets configuration and provide a practical basis for assessing hotspot risks and guiding airflow optimization solutions for battery cooling systems in real-world applications, we have compiled the average temperature of each cell in Table 6:

In this model, the distribution of gas flow velocity changes significantly compared to the base case as evidenced in Figure 8. The gas flow supplied from two inlets creates local acceleration zones in front of the cell rows near the inlet, while forming vortices along the side walls and in the gaps between the cells. Turbulence increases in the central region, helping to break up the "thermal boundary layer" and enhance convective heat transfer. In particular, the appearance of vortices after the first and second rows of cells contributes to the redistribution of the gas flow, reducing the lack of circulation in the middle of the cell module, which is the cause of hot spots in the 1 inlet-1 outlet configuration.

As a result, overall cooling efficiency is significantly improved, as evidenced by the reduction in maximum temperature and the decrease in temperature difference between cells. However, large vortices near the side walls may also increase pressure losses, which should be considered when evaluating the system's energy efficiency. In contrast, ΔT_{max} still exceeds the recommended threshold of 5 K for practical applications, indicating that further research is needed to develop additional solutions to improve the temperature difference to a better level.

3.1.3 2-inlet, 2-outlet model, counterflow airflow

In this model, simulation results show a significant decrease in cooling performance compared to other configurations. The velocity field distribution is shown in Figure 9 to demonstrate the existence of recirculation zones and the phenomenon of short-circuited airflow: When two cold air streams enter from opposite sides and meet in the central region, the opposing momentum generates recirculation zones and a stagnation zone. These phenomena cause the effective velocity to decrease sharply in the center of the module, reducing the convective heat transfer coefficient and leading to localized heat accumulation. At the same time, the airflow along the side walls tends to escape quickly through the nearest outlets, causing short-circuit flow and bypassing the center. As a result, the central cells (2-3, 3-3, 2-4, 3-4) reach the highest temperatures, while the inlet-side cells maintain lower temperatures. As a result, both the maximum temperature and the average temperature across the entire module in this case are significantly higher than in the same-direction configuration. This is clearly shown in the temperature distribution field in Figure 10, where the center of the module shows clusters of dark red cells, corresponding to temperatures significantly higher than the edge cells. To illustrate this heat accumulation phenomenon in more detail, we calculated the average temperature of each cell and compared the differences

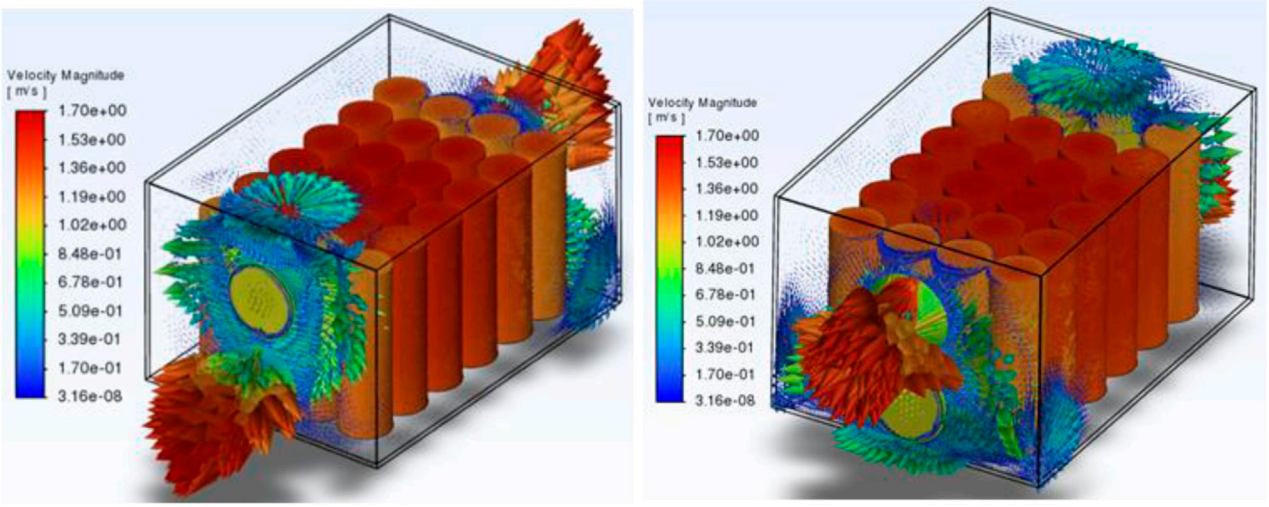

FIGURE 9
Airflow velocity distribution in the 2 inlets – 2 outlets module, with counterflow airflow.

between the center and edge regions. The results are presented in Table 7.

The results in Table 7 show that the average temperature of each cell in the 2-inlet, 2-outlet configuration with counter-flow gas and no partition is unevenly distributed, with the lowest value reaching 323.584 K at cell 2-1 and the highest reaching 333.201 K at cell 3-3. Thus, the maximum temperature difference between cells, ΔT_{max} = 9.6 K, is slightly lower than in the two-inlet, two-outlet co-flow configuration, where ΔT_{max} is only about 9.9 K, but T_{max} is nearly 13 K lower. The increase in T_{max} and ΔT_{max} shows little reduction in this configuration, indicating that arranging two opposing airflows without a directional partition does not provide effective cooling; on the contrary, it reduces the ability to evenly distribute heat within the module.

This confirms that flow opposition in the partitionless configuration is the direct cause of the simultaneous increase in T_{max}. Based on this result, the study opens up a direction for improvement by adding a central partition to separate the two air streams, preventing stagnation zones and forcing the cooling air stream to pass through the channels between the cells before exiting the outlet. This is an important basis for developing configurations in the next group with higher and more uniform cooling performance.

3.2 Cooling performance of the model with additional partitions

3.2.1 2 inlets – 2 outlets model, cooling air flows in the same direction

Although the results for the 2 inlets-2 outlets configuration with parallel flow and no partition (3.1.2) show that the maximum temperature has decreased compared to the base model, the heat distribution is still uneven. ΔT_{max} is still quite large, and hot spots are still concentrated in the central area. Hence, in this configuration, we will add partitions to direct the airflow through the gaps between the cells, reduce short-circuit flow, increase the local velocity of the cooling airflow, and improve heat exchange efficiency in the central area as presented in Figure 11. The baffles are arranged along the length of the module, positioned between the height of the cell and dividing the airflow space into two separate channels, thereby forcing the cold airflow to pass through the gaps between the cells instead of preferentially following the shell to quickly escape through the outlet. First, we add baffles to the 2-airflow configuration to evaluate the degree of improvement when applying this solution.

When analyzing the velocity field, it can be observed that in the 2-inlet, 2-outlet configuration with no partitions, the gas flow tends to follow the shell wall to exit the outlet, creating local vortices on the side walls and short-circuit flow phenomena at the gaps between cells. The average velocity in the central region only reaches about 0.35–0.45 m/s, which is much lower than the rated velocity at the inlet, leading to limited convective heat transfer in this region.

Conversely, in the partitioned configuration, the airflow is forced to pass through narrow channels between the cells before escaping, thereby creating a significant increase in local velocity. The average velocity in the central region increases to 0.55–0.65 m/s, which is approximately 30%–40% higher than in the configuration without partitions. This phenomenon helps break the thermal boundary layer while increasing the convective heat transfer coefficient in the central cells, which are typical hot spots in previous models. In terms of temperature, the difference is even more pronounced. The temperature distribution and average temperature of each battery cell are shown in Figure 12 and Table 8. In the configuration without partitions, the maximum temperature reaches 320.715 K, the minimum temperature is 310.893 K, resulting in a $\Delta T_{max} \approx 9.9$ K. Meanwhile, in the partitioned configuration, the maximum temperature decreased

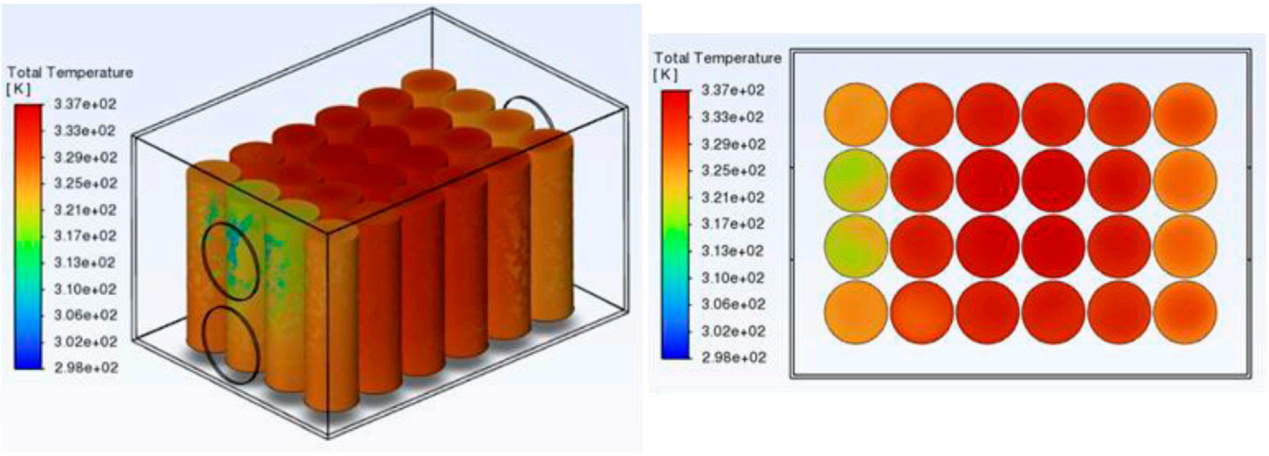

FIGURE 10
Temperature distribution in the module with 2 inlets and 2 outlets, counterflow airflow.

TABLE 7 Average temperature of each battery cell.

Cell	T (K)	Cell	T (K)	Cell	T (K)	Cell	T (K)
1-1	326.248	2-1	323.584	3-1	323.738	4-1	326.337
1-2	330.598	2-2	330.959	3-2	331.019	4-2	330.609
1-3	331.872	2-3	333.197	3-3	333.201	4-3	331.783
1-4	331.387	2-4	332.949	3-4	332.936	4-4	331.353
1-5	329.443	2-5	330.479	3-5	330.509	4-5	329.509
1-6	325.945	2-6	324.669	3-6	324.686	4-6	326.034

to 317.924 K, and the minimum temperature increased to 312.011 K, resulting in a ΔT_{max} of 5.9 K.

Thus, compared to the case without a partition, T_{max} decreases by approximately 2.8 K (equivalent to 5.8%), T_{min} increases by approximately 1.1 K (≈2.9%), and ΔT_{max} decreases by 39.8%. This is a significant improvement, demonstrating the combined effect of lowering the maximum temperature and narrowing the temperature difference, two key parameters in ensuring the safe operation of the battery module.

After demonstrating the significant improvement in efficiency of the baffle in the 2-inlet, 2-outlet configuration, an important question arises: Does the combination of the baffle and counterflow provide similar or even superior efficiency? In the configuration without a baffle, counterflow exhibited major limitations due to the appearance of stagnation zones and recirculation phenomena, causing the maximum temperature to increase and ΔT_{max} to remain unchanged. For this reason, adding partitions in this case is expected to address the above shortcomings by separating and redirecting the airflow, forcing the air to pass through the gaps between the cells, and avoiding short-circuit flow in the central region. Therefore, in the next section, we conduct a detailed survey of the cooling performance of the 2-inlet, 2-outlet counterflow configuration with a partition, in order to directly compare it with both the counterflow case without a partition and the co-flow case with a partition. These results will allow for a more comprehensive assessment of the role of the partition in controlling the temperature field and velocity field under the influence of two opposing airflow directions.

3.2.2 2-inlet, 2-outlet model with partition, counterflow

The simulation results of the 2-inlet, 2-outlet counterflow configuration with partitions show a significant improvement compared to the case without partitions. Observing the velocity field in Figure 13, it is evident that the partitions play a guiding role, forcing the gas flow to pass through the narrow gaps between the cells instead of directly opposing each other at the center as in configuration 3.1.3. As a result, large stagnation and recirculation zones at the center were eliminated, replaced by stable flow channels with average velocities of approximately 0.5–0.6 m/s, nearly 50% higher than in the counterflow case without a partition. The short-circuit flow phenomenon along the side walls no longer appears significantly, helping to distribute the airflow more evenly throughout the entire module.

The change in flow characteristics directly affected the temperature distribution, as shown in Figure 14. Observe the statistical table of the average temperature of each cell in the module, shown in Table 9. The maximum temperature of the battery cells was only 314.768 K at cells 2-3 and 3-3, a decrease of more than 18 K compared to the opposite case without a partition (333.201 K), and also nearly 3 K lower than the same configuration with a partition. The minimum temperature reached 311.870 K at cells 1-6 and 4-6, equivalent to the results in 3.2.1 and much lower than configuration 3.1.3. Most notably, the maximum temperature difference ΔT_{max} across the entire module is only about 2.9 K, a reduction of nearly 70% compared to the opposite-direction configuration without partitions and nearly half that of the same-direction configuration with partitions. This demonstrates not only a reduction in maximum temperature but also a significant improvement in thermal uniformity within the module.

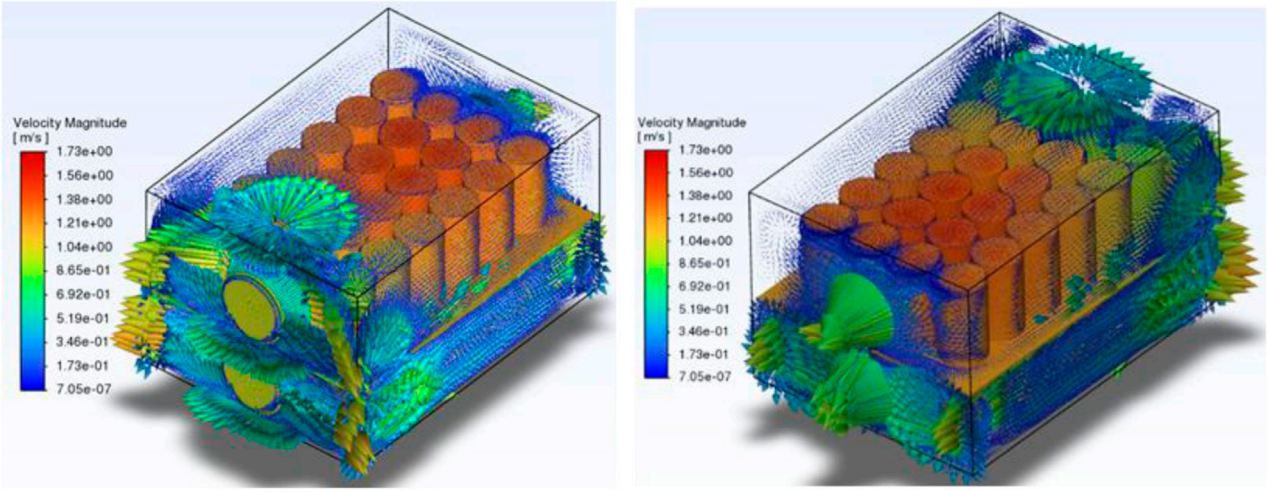

FIGURE 11
Distribution of gas flow velocity in the module.

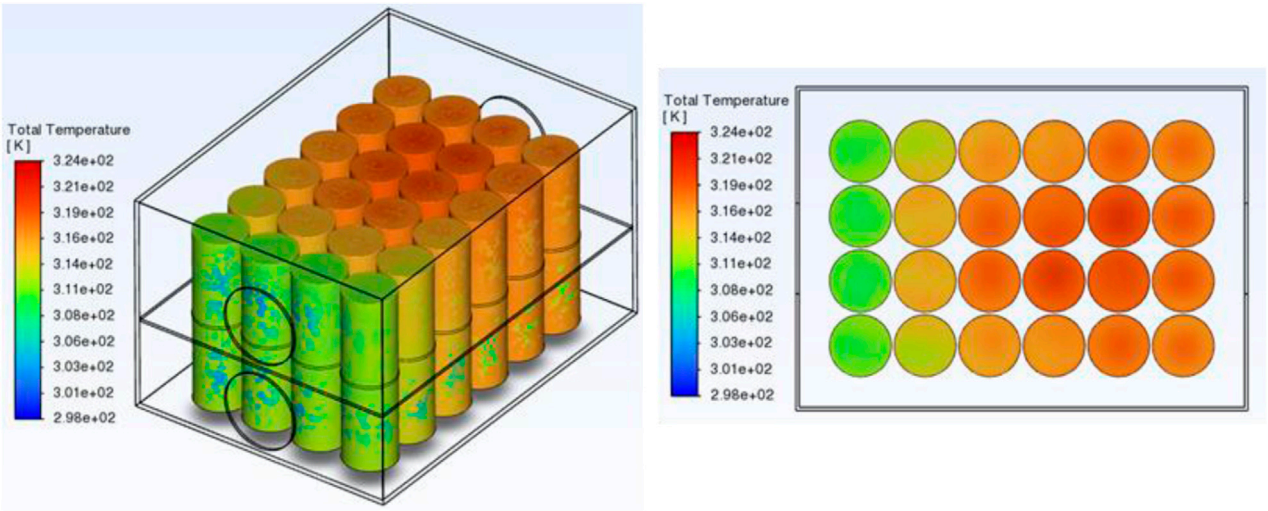

FIGURE 12
Temperature distribution on the 2 inlets-2 outlets module with a partition in between, with the airflow entering in the same direction.

TABLE 8 Average temperature of each battery cell.

Cell	T (K)	Cell	T (K)	Cell	T (K)	Cell	T (K)
1-1	312.139	2-1	312.026	3-1	312.011	4-1	312.134
1-2	314.195	2-2	314.812	3-2	314.815	4-2	314.187
1-3	315.659	2-3	316.656	3-3	316.652	4-3	315.650
1-4	316.589	2-4	317.662	3-4	317.661	4-4	316.572
1-5	316.925	2-5	317.924	3-5	317.921	4-5	316.917
1-6	316.533	2-6	317.212	3-6	317.210	4-6	316.529

Thus, configuration 3.2.2 completely overcomes the limitations inherent in 3.1.3 and improves cooling performance over the configuration in Section 3.2.1. In the counterflow model without partitions, the central region often overheats due to counterflow and recirculation. However, with the introduction of partitions, the central cells become the most effectively cooled area thanks to increased airflow velocity and uniform distribution. Compared to the same-direction configuration with a partition, case 3.2.2 also demonstrates a significant advantage in temperature uniformity, reducing ΔT_{max} to below 3 K–an ideal value in the design of air-based BTMS systems.

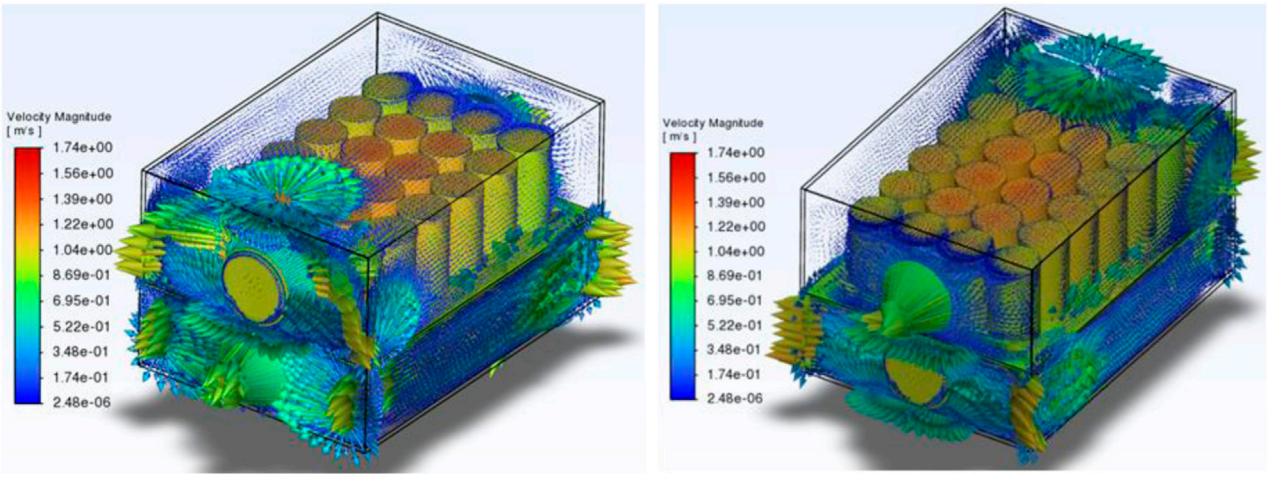

FIGURE 13
Airflow velocity distribution in the module.

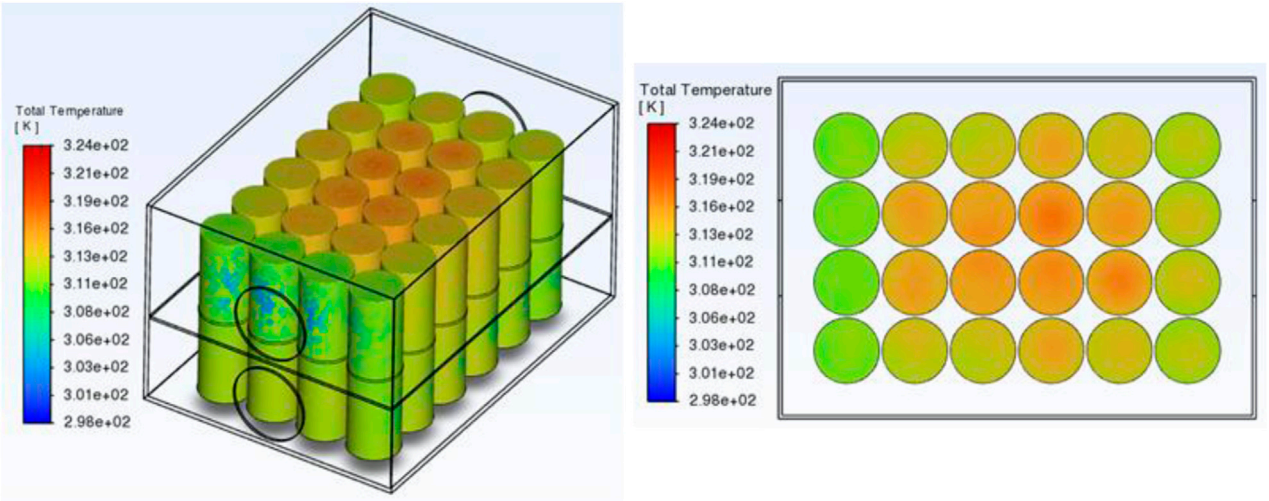

FIGURE 14
Temperature distribution in the module.

TABLE 9 Average temperature of each battery cell in the module.

Cell	T (K)	Cell	T (K)	Cell	T (K)	Cell	T (K)
1-1	311.920	2-1	312.160	3-1	312.145	4-1	311.920
1-2	313.219	2-2	314.036	3-2	314.038	4-2	313.216
1-3	313.717	2-3	314.767	3-3	314.768	4-3	313.715
1-4	313.631	2-4	314.655	3-4	314.658	4-4	313.624
1-5	313.012	2-5	313.839	3-5	313.841	4-5	313.010
1-6	311.870	2-6	312.267	3-6	312.274	4-6	311.873

3.3 Analysis of pressure drop and fan power consumption

In addition to thermal performance, pressure loss is also an important factor for comprehensively evaluating cooling systems. The pressure difference between the inlet and outlet of the module directly determines the required cooling fan power. Therefore, analyzing ΔP along with cooling performance is necessary to determine the optimal configuration, balancing thermal control capabilities and energy feasibility.

TABLE 10 Cooling performance and energy loss statistics between configurations.

Case	Description	T_{max} (K)	$P_{in\text{-}avg}$ (Pa)	$P_{out\text{-}avg}$ (Pa)	ΔP (Pa)	Estimated fan power, P (W)
1	1 inlet – 1 outlet (base)	346.852	3.386	1.339	2.047	4.265×10^{-3}
2	2 inlets - 2 outlets, same airflow direction	320.715	2.984	1.194	1.79	3.73×10^{-3}
3	2 inlets - 2 outlets, counterflow	333.201	2.254	1.112	1.142	2.38×10^{-3}
4	Co-flow, with partition	317.924	3.494	1.199	2.295	4.781×10^{-3}
5	Counterflow, with partition	314.768	3.497	1.196	2.301	4.794×10^{-3}

Based on the methodology presented, the corresponding ΔP values and fan power for each case have been determined. These results, along with the temperature criteria, are summarized in Table 10.

Analysis of the data from Table 10 shows a marked difference in pressure loss and fan power between the configurations, reflecting a direct correlation between cooling performance and energy loss.

The configurations with partitions (Case 4 and Case 5) recorded the highest ΔP and P values, reaching 2,295 Pa – 4.781×10^{-3} W and 2,301 Pa – 4.794×10^{-3} W, respectively. This increase stems from the partitions forcing the airflow through narrow gaps between the cells, increasing friction and local losses. However, this very mechanism contributes to enhancing heat exchange efficiency by directing the flow and breaking the thermal boundary layer, as discussed in previous sections. Conversely, the unpartitioned reverse flow configuration (Case 3) has the lowest ΔP and P, at 1.142 Pa and 2.38×10^{-3} W, respectively, due to the formation of stagnation zones and large recirculation zones, which reduce overall friction losses. This characteristic leads to poor heat dissipation, as evidenced by T_{max} = 333.201 K–the highest in the non-partitioned group. Comparing the two non-partitioned configurations, Case 2 has a higher ΔP and P (1.79 Pa) but achieves significantly better cooling efficiency with T_{max} = 320.715 K.

The detailed comparison of the cooling configurations reveals three distinct design trade-offs. First, partitioned configurations exhibit the highest ΔP and fan power due to the forced airflow through narrow channels, yet they yield the superior thermal uniformity. Second, the unpartitioned counter-flow case results in the lowest pressure drop but simultaneously shows the highest T_{max} in the non-partitioned group due to internal stagnation zones. Third, the unpartitioned co-flow configuration offers a balanced trade-off, achieving significantly improved cooling efficiency over Case 3 with only a moderate pressure loss. The selection of the optimal configuration, therefore, requires balancing thermal control capability and energy costs, which will be analyzed in detail in the next section.

3.4 Evaluate the optimal configuration

To determine the optimal cooling configuration, the models were compared based on three criteria: thermal performance, energy efficiency, and design feasibility. Thermal performance is evaluated through the time variation of the maximum temperature T_{max} and the maximum temperature difference ΔT_{max}, reflecting the ability to control hot spots and maintain a uniform thermal field, with the target ΔT_{max} <5 K. Energy efficiency is determined from pressure loss and fan power, while feasibility is considered through the number of inlets/outlets and partition structure affecting manufacturability and practical application.

3.4.1 Compare T_{max} and ΔT_{max} over time

Figures 15, 16 illustrate the temporal evolution of maximum temperature and the largest temperature difference for the five survey configurations. The results show that all configurations undergo two typical phases: an initial rapid increase phase due to the transient effect and a stable phase when convection reaches equilibrium. On the other hand, the rate of temperature increase, stable values, and time to reach a stable state differ significantly between configurations, reflecting differences in flow characteristics and heat transfer efficiency.

Regarding maximum temperature, Case 1 (base model) has the fastest increase rate and reaches a stable state after 151 s with T_{max} = 346.852 K–the highest in the group, indicating poor heat dissipation and strong heat accumulation in the central region. Case 2 (2 inlets-2 outlets, same direction, no partition) reaches T_{max} = 320.715 K and stabilizes after 195 s, showing better cooling efficiency but high thermal inertia. Case 3 (opposite direction, no partition) stabilizes earlier at 134 s but still has T_{max} = 333.201 K due to the counterflow reducing heat exchange in the central region.

The two configurations with partitions demonstrate superior performance. Case 4 (same direction, with partition) achieves stability at 140 s with T_{max} = 317.924 K, proving that the partition helps direct the airflow and break the thermal boundary layer. Case 5 is the optimal configuration, achieving T_{max} = 314.768 K–the lowest, and the fastest stabilization time of 101 s. The combination of counterflow and partitions helps maintain high velocity, distribute air evenly, and enhance thermal convection throughout the module.

In terms of the maximum temperature difference, the variation trend is similar to T_{max} but shows a clearer degree of thermal uniformity. Case 1 has ΔT_{max} = 39.7 K, far exceeding the permissible threshold of 5 K. Cases 2 and 3 achieve 9.9 K and 9.6 K, respectively, showing improvement but still failing to meet design requirements. Case 4 reduces to 5.9 K, indicating a more reasonable airflow distribution, while Case 5 drops to 2.9 K and achieves stability earliest, demonstrating near-perfect thermal uniformity throughout the entire module.

In summary, Case 5 demonstrates clear superiority across both thermal stability metrics. Based on the lowest final T_{max} and the fastest stabilization time in the transient phase, the thermal performance ranking from best to worst is: Case 5 > Case 4 > Case 2 > Case 3 > Case 1. This ranking unequivocally reinforces the

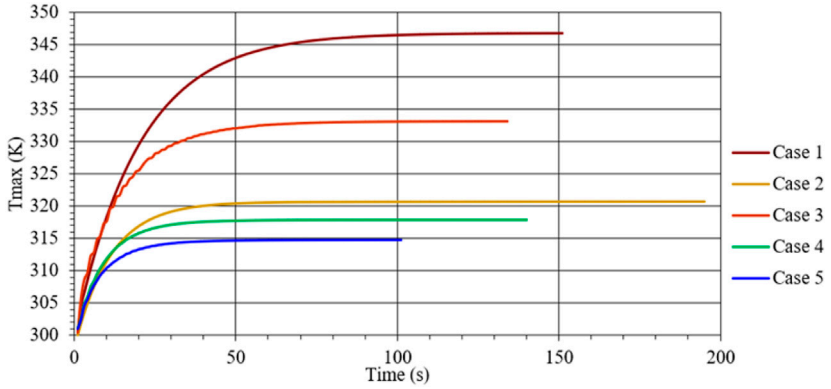

FIGURE 15
T_{max} evolution over time for the cooling models.

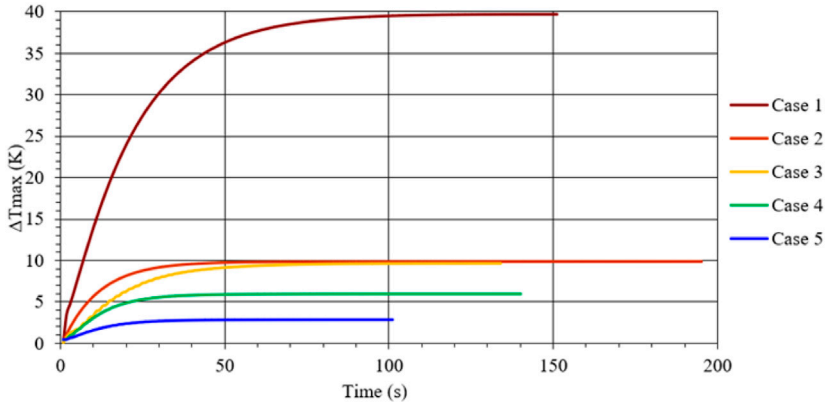

FIGURE 16
ΔT_{max} over time for the cooling models.

effectiveness of combining counter-flow configuration with internal partitions for achieving optimal BTMS thermal control.

3.4.2 Quantitative assessment of improvement level

Regarding maximum temperature targets: All configurations show a clear downward trend compared to Case 1, with Case 5 achieving the largest reduction of 9.25%, followed by Case 4 at 8.34% and Case 2 at 7.54%. Case 3 only achieved 3.94%, showing almost no significant improvement, proving that simply changing the flow direction without adding baffles is insufficient to create a difference in cooling performance.

In terms of the maximum temperature difference: All configurations have very high NRR, demonstrating a significant improvement over the baseline. Case 5 stands out with a ΔT_{max} reduction of up to 92.70%, nearly eliminating hotspots entirely. Case 4 also achieves high efficiency with a reduction of 85.14% compared to Case 1, while Case 2 and Case 3 stop at around 75%, showing the limitations of configurations without partitions in evenly distributing airflow.

Concerning fan power, the results show that Case 2 and Case 3 have positive energy improvements of 12.54% and 44.20%, respectively, due to the simpler flow configuration and lower pressure losses. However, these cases offer lower thermal gains and consequently higher T_{max} compared to the partitioned configurations. Conversely, Case 4 and Case 5 recorded negative values of −12.10% and −12.40%, respectively, reflecting increased pressure losses due to the presence of partitions and branched airflow. Nevertheless, this reduction is still within acceptable limits when considering the superior thermal benefits achieved.

With reference to manufacturing feasibility, the configurations using two inlets and two outlets require parallel air duct arrangements but are still feasible in practice due to their simple structure and ease of installation. Furthermore, the partitions can be fabricated from thin aluminum sheets at low cost, enabling efficient airflow direction without significantly increasing manufacturing complexity. Crucially, the substantial benefits achieved in terms of thermal uniformity and extended battery life fully offset the increased fabrication cost.

The summary of results shows that Case 5 is the optimal configuration, achieving an outstanding balance between maximum temperature reduction, maintaining a uniform thermal field, and acceptable energy consumption as shown in Figure 17. Case 5 demonstrated superior thermal performance, achieving a

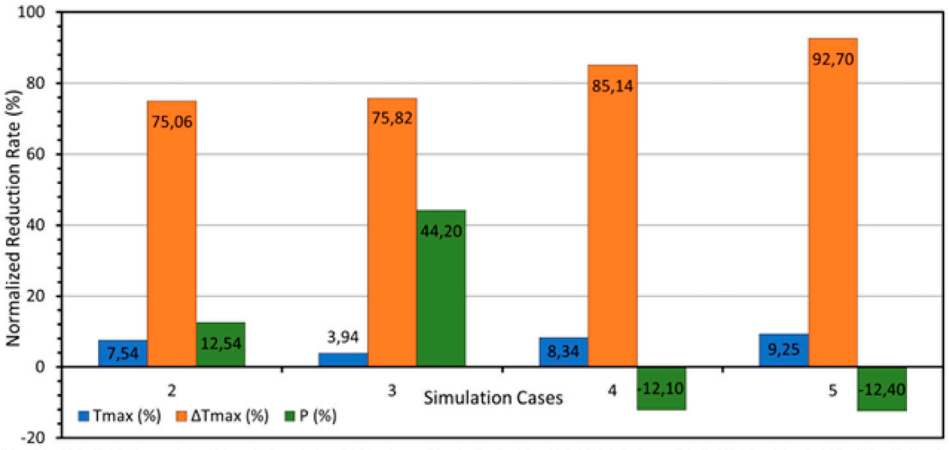

FIGURE 17
Normalized reduction rate of all simulation cases.

9.25% reduction in T_{max} and an exceptional 92.70% reduction in ΔT_{max} compared to the base configuration. While the open configurations, Case 2 and 3, demonstrate a trade-off between thermal efficiency and energy consumption, the configurations with partitions, particularly Case 5, have proven to be comprehensive in both performance and thermal stability.

4 Conclusion

Based on simulation and analysis results, the study revealed the crucial role of airflow configuration and internal partitions in the thermal performance of the 4 × 6-cell lithium-ion battery module. The main conclusions are summarized as follows:

1. Configuration with two inlets and two outlets, the counterflow with baffles (Case 5) demonstrated superior performance, reducing the maximum temperature from 346.852 K to 314.768 K (a 9.25% decrease) and the temperature difference between cells from 39.7 K to only 2.9 K (a 92.7% decrease). This proves that adding partitions combined with counter-current flow can effectively control hot spots while significantly improving thermal uniformity throughout the module. The significant thermal uniformity achieved is crucial for promoting battery lifespan and substantially reducing the risk of thermal runaway, thereby ensuring safer battery operation in practical applications.
2. Configurations with partitions provide significant cooling efficiency but increase pressure loss and fan power consumption by approximately 10%–12% compared to the base configuration. However, this increase remains within acceptable limits, reflecting the natural trade-off between heat dissipation capability, energy loss, and design feasibility in BTMS systems. Therefore, the counter-flow configuration with baffles (Case 5) provides the best overall compromise among thermal uniformity, hotspot mitigation, and acceptable energy consumption.
3. The modeling approach was successfully validated through independent grid assessment, and the use of Bernardi's thermal model ensured the stability, accuracy, and applicability of the results for multi-cell modules. The results provide important guidance for the design of air-cooled systems with simple structures and low costs that still meet real-world thermal control requirements.

Nevertheless, the study still has certain limitations: the simulations were performed under stable conditions, with a fixed discharge rate of 3C, without considering the effects of thermal radiation, actual environmental conditions, and the nonlinear characteristics of the cooling fan. In addition, the heat generation model was assumed to be uniform, not reflecting the actual non-uniformity within each cell. In subsequent studies, we will combine CFD simulations with experiments to validate the results, develop a nonlinear heat generation model, and optimize the baffle geometry and consider integration with other advanced cooling strategies (e.g., liquid cooling or PCM-based systems) to further improve the energy efficiency and practical applicability of the air-based BTMS system.

Data availability statement

The original contributions presented in the study are included in the article/Supplementary Material, further inquiries can be directed to the corresponding author.

Author contributions

MP: Conceptualization, Data curation, Formal Analysis, Investigation, Methodology, Project administration, Software, Supervision, Validation, Visualization, Writing – original draft, Writing – review and editing. T-CC: Supervision, Validation, Visualization, Investigation, Writing – review and editing. DC: Conceptualization, Supervision, Writing – original draft, Writing – review and editing. HN: Conceptualization, Data curation, Investigation, Methodology, Writing – original draft, Writing – review and editing. VD: Conceptualization, Data curation, Formal Analysis, Investigation, Methodology, Software, Supervision, Validation, Writing – original draft, Writing – review and editing. ND:

Conceptualization, Data curation, Formal Analysis, Investigation, Methodology, Software, Validation, Writing – original draft, Writing – review and editing. HP: Conceptualization, Methodology, Software, Supervision, Writing – original draft, Writing – review and editing. DN: Conceptualization, Data curation, Formal Analysis, Investigation, Methodology, Software, Supervision, Writing – original draft, Writing – review and editing, Validation, Visualization.

Funding

The author(s) declared that financial support was not received for this work and/or its publication.

Conflict of interest

The author(s) declared that this work was conducted in the absence of any commercial or financial relationships that could be construed as a potential conflict of interest.

Generative AI statement

The author(s) declared that generative AI was not used in the creation of this manuscript.

Any alternative text (alt text) provided alongside figures in this article has been generated by Frontiers with the support of artificial intelligence and reasonable efforts have been made to ensure accuracy, including review by the authors wherever possible. If you identify any issues, please contact us.

Publisher's note

References

Aghajan-Eshkevari, S., Azad, S., Nazari-Heris, M., Ameli, M. T., and Asadi, S. (2022). Charging and discharging of electric vehicles in power systems: an updated and detailed review of methods, control structures, objectives, and optimization methodologies. *Sustainability* 14 (4), 2137. doi:10.3390/su14042137

Al-Zareer, M., Dincer, I., and Rosen, M. A. (2018). A review of novel thermal management systems for batteries. *Int. J. Energy Res.* 42 (10), 3182–3205. doi:10.1002/er.4095

ANSYS, Inc. (2025). *ANSYS fluent theory guide (2025 R1)*. Canonsburg, PA.

Argade, S., and De, A. (2024). Optimization study of a Z-type airflow cooling system of a lithium-ion battery pack. *Phys. Fluids* 36 (6), 067119. doi:10.1063/5.0212606

Bamrah, P., Chauhan, M. K., and Sikarwar, B. S. (2022). CFD analysis of battery thermal management system. *J. Phys. Conf. Ser.* 2178 (1), 012035. doi:10.1088/1742-6596/2178/1/012035

Chen, T., Jin, Y., Lv, H., Yang, A., Liu, M., Chen, B., et al. (2020). Applications of lithium-ion batteries in grid-scale energy storage systems. *Trans. Tianjin Univ.* 26 (3), 208–217. doi:10.1007/s12209-020-00236-w

Chen, K., Zhang, Z., Wu, B., Song, M., and Wu, X. (2024). An air-cooled system with a control strategy for efficient battery thermal management. *Appl. Therm. Eng.* 236, 121578. doi:10.1016/j.applthermaleng.2023.121578

Elmahallawy, M., Elfouly, T., Alouani, A., and Massoud, A. M. (2022). A comprehensive review of lithium-ion batteries modeling, and state of health and remaining useful lifetime prediction. *IEEE Access* 10, 119040–119070. doi:10.1109/access.2022.3221137

Feng, X., Ren, D., He, X., and Ouyang, M. (2020). Mitigating thermal runaway of lithium-ion batteries. *Joule* 4 (4), 743–770. doi:10.1016/j.joule.2020.02.010

Hmidi, N., Merrouni, A. A., Panchal, S., Fraser, R., Fowler, M., Amrani, A. I., et al. (2026). Enhanced battery thermal management using nano-PCM, copper foam, and aluminum minichannels: an optimized hybrid approach. *J. Energy Storage* 141, 119307. doi:10.1016/j.est.2025.119307

Jin, S., Youn, M. S., and Kim, Y. J. (2021). "Optimization of air-cooling system for a lithium-ion battery pack." *E3S Web Conf.* Paris, France: EDP Sciences 321, 02018. doi:10.1051/e3sconf/202132102018

Khan, J., Jan, S., Ifitkhar, S., Yaqoob, A., Rehman, U. U., Cheema, T. A., et al. (2025). Design and performance optimization of battery pack with AI-Driven thermal runaway prediction. *Mater. Proc.* 23 (1), 17. doi:10.3390/materproc2025023017

Koorata, P. K., and Chandrasekaran, N. (2021). Numerical investigation of cooling performance of a novel air-cooled thermal management system for cylindrical Li-ion battery module. *Appl. Therm. Eng.* 193, 116961. doi:10.1016/j.applthermaleng.2021.116961

Li, S., Wang, K., Zhang, G., Li, S., Xu, Y., Zhang, X., et al. (2022). Fast charging anode materials for lithium-ion batteries: current status and perspectives. *Adv. Funct. Mater.* 32 (23), 2200796. doi:10.1002/adfm.202200796

Li, X., Liu, J., and Li, X. (2024). A Y-Type air-cooled battery thermal management system with a short airflow path for temperature uniformity. *Batteries* 10 (9), 302. doi:10.3390/batteries10090302

Lin, J., Liu, X., Li, S., Zhang, C., and Yang, S. (2021). A review on recent progress, challenges and perspective of battery thermal management system. *Int. J. Heat Mass Transf.* 167, 120834. doi:10.1016/j.ijheatmasstransfer.2020.120834

Lin, D., Peng, P., Wang, Y., Qiu, Y., Wu, W., and Jiang, F. (2024). Numerical investigation of the thermal performance of air-cooling system for a lithium-ion battery module combined with epoxy resin boards. *Batteries* 10 (9), 318. doi:10.3390/batteries10090318

Madani, S. S., Shabeer, Y., Nair, A. S., Fowler, M., Panchal, S., Ziebert, C., et al. (2025). Advances in battery modeling and management systems: a comprehensive review of techniques, challenges, and future perspectives. *Batteries* 11 (11), 426. doi:10.3390/batteries11110426

Makings, M., Maciocha, M., Biggs, J., Salek, F., Zare, A., and Resalati, S. (2024). CFD analysis of the battery thermal management system for a heavy-duty truck (No. 2024-01-2668). SAE Technical Paper.

Masthan Vali, P. S. N., Murali, G., and Kurhade, A. S. (2025). Simulation-based evaluation of battery thermal management systems for cylindrical Li-Ion batteries in electric vehicles. *J. Mines Metals Fuels* 73 (3), 555–570. doi:10.18311/jmmf/2025/48185

Mohapatra, J. R., Moharana, M. K., and Panchal, S. (2025). Indirect liquid-cooled lithium-ion battery module with improved circuitous minichannel cold plate design: a numerical study involving the effect of different flow configurations. *J. Therm. Analysis Calorim.* 150, 1–28. doi:10.1007/s10973-025-14647-1

Muenzel, V., Hollenkamp, A. F., Bhatt, A. I., de Hoog, J., Brazil, M., Thomas, D. A., et al. (2015). A comparative testing study of commercial 18650-format lithium-ion battery cells. *J. Electrochem. Soc.* 162 (8), A1592–A1600. doi:10.1149/2.0721508jes

Murphy, M., and Akrami, M. (2024). Advanced thermal management of cylindrical lithium-ion battery packs in electric vehicles: a comparative CFD study of vertical, horizontal, and optimised liquid cooling designs. *Batteries* 10 (8), 264. doi:10.3390/batteries10080264

Murugan, M., Elumalai, P. V., Vijayakumar, K. C. K., Babu, M., Suresh Kumar, K., Ganesh, M., et al. (2025). A comprehensive review of thermal management methods and ideal system design for improved electric vehicle battery pack performance and safety. *Energy Sci. Eng.* 13 (3), 1011–1036. doi:10.1002/ese3.2081

Mustafa, J. (2022). Effect of inlet and outlet size, battery distance, and air inlet and outlet position on the cooling of a lithium-ion battery pack and utilizing outlet air of cooling system to heat an air handling unit. *J. Energy Storage* 46, 103826. doi:10.1016/j.est.2021.103826

Na, X., Kang, H., Wang, T., and Wang, Y. (2018). Reverse layered air flow for Li-ion battery thermal management. *Appl. Therm. Eng.* 143, 257–262. doi:10.1016/j.applthermaleng.2018.07.080

Narkhede, S., Sur, A., Kothari, G., and Netke, A. (2025). Design and thermal analysis of Fin-PCM-integrated thermal management system for lithium-ion cylindrical battery pack. *Proc. Institution Mech. Eng. Part E J. Process Mech. Eng.* 239 (6), 3269–3278. doi:10.1177/09544089231221668

Nicholls, R. (2024). *Lithium-ion 18650 cylindrical battery thermal management: multi-level CFD simulations utilising phase change materials for enhanced performance*. Stoke-on-Trent, United Kingdom: University of Staffordshire.

Oyewola, O. M., Idowu, E. T., and Drabo, M. L. (2024). Influence of straight and inclined baffles on enhancement of battery thermal management system performance. *Heliyon* 10 (19), e38585. doi:10.1016/j.heliyon.2024.e38585

Peng, X., Cui, X., Liao, X., and Garg, A. (2020). A thermal investigation and optimization of an air-cooled lithium-ion battery pack. *Energies* 13 (11), 2956. doi:10.3390/en13112956

Pham, M., Kien, N. T., Hung, C. D., and Long, L. D. (2025). Evaluation of the effectiveness of cooling channel parameters on thermal performance for electric vehicles using cylindrical lithium-ion batteries. *J. Phys. Conf. Ser.* Bristol, United Kingdom: IOP Publishing 2968, 1012013. doi:10.1088/1742-6596/2968/1/012013

Qian, L., Yi, Y., Zhang, W., Fu, C., Xia, C., and Ma, T. (2023). Revealing the impact of high current overcharge/overdischarge on the thermal safety of degraded li-ion batteries. *Int. J. Energy Res.* 2023 (1), 8571535. doi:10.1155/2023/8571535

Sarvestani, A. B., Vakilzadeh, A. H., Javaherdeh, K., Kamali, R., and Panchal, S. (2025). 3D numerical study of a novel fan-shaped heat sink with triangular cavities and nano-enhanced PCMs. *Appl. Therm. Eng.* 280, 128408. doi:10.1016/j.applthermaleng.2025.128408

Satheesh, V. K., Krıshna, N., Kushwah, P. S., Garg, I., Raı, S., Hebbar, G. S., et al. (2021). Enhancement in air-cooling of lithium-ion battery packs using tapered airflow duct. *J. Therm. Eng.* 10 (2), 375–385. doi:10.18186/thermal.1448648

Sur, A., Narkhede, S., Netke, A., and Palheriya, H. (2023). "Design and analysis of polymer heat sink for Li-Ion battery thermal management system," in *Recent trends in mechanical engineering: select proceedings of PRIME 2021* (Singapore: Springer Nature Singapore), 323–329.

Xie, Y., Ma, W., Jiang, D., Li, W., Yang, H., Panchal, S., et al. (2025). A high-fidelity online monitoring algorithm for multiple physical fields in battery pack. *Appl. Energy* 398, 126443. doi:10.1016/j.apenergy.2025.126443

Zhang, H., Li, C., Zhang, R., Lin, Y., and Fang, H. (2020). Thermal analysis of a 6s4p lithium-ion battery pack cooled by cold plates based on a multi-domain modeling framework. *Appl. Therm. Eng.* 173, 115216. doi:10.1016/j.applthermaleng.2020.115216

Zhang, F., Liu, P., He, Y., and Li, S. (2022). Cooling performance optimization of air cooling lithium-ion battery thermal management system based on multiple secondary outlets and baffle. *J. Energy Storage* 52, 104678. doi:10.1016/j.est.2022.104678

Zhang, F., Shi, Y., He, Y., and Liu, P. (2023). Design and optimization of an F-type air-cooling structure for lithium-ion battery of electric vehicle. *Energy Technol.* 11 (9), 2300243. doi:10.1002/ente.202300243

Zhao, G., Wang, X., and Negnevitsky, M. (2021). A study of variable cell spacings to the heat transfer efficiency of air-cooling battery thermal management system. *Appl. Sci.* 11 (23), 11155. doi:10.3390/app112311155

Zhao, G., Wang, X., Negnevitsky, M., and Zhang, H. (2023). A design optimization study of an air-cooling battery thermal management system for electric vehicles. *Proc. Institution Mech. Eng. Part E J. Process Mech. Eng.* 237 (4), 1125–1136. doi:10.1177/09544089221116418

Zhu, X., Wang, Z., Wang, H., and Wang, C. (2020). Review of thermal runaway and safety management for lithium-ion traction batteries in electric vehicles. *J. Mech. Eng.* 56 (14), 91–118. doi:10.3901/jme.2020.14.091

10.3389/fmech.2025.1743715

Glossary

Q (W)	Heat generation
Q (m^3/s)	Total airflow rate
v (V)	Cell voltage
v (m/s)	Air velocity
v_{ocv} (V)	Open-circuit voltage
I (V)	Discharge current
T (K/°C)	Temperature
T_{max} (K)	Maximum module temperature
ΔT_{max} (K)	Maximum temperature difference
Q_t (W/m^3)	Heat generation coefficient per volume
R (Ω)	Internal resistance
R_e	Reynolds number
ρ (kg/m^3)	Density (air)
μ (Pa·s)	Dynamic viscosity (air)
k (m^2/s^2)	Turbulent kinetic energy
ε (m^2/s^3)	Turbulent dissipation rate
η	Fan efficiency
ΔP (Pa)	Pressure drop
P (W)	Fan power
D (m)	Characteristic hydraulic diameter
μ_t (Pa·s)	Turbulent (eddy) viscosity
Δt (s)	Time step
C_p (J/kg·K)	Specific heat capacity
k (W/m·K)	Thermal conductivity
in, out	Inlet/Outlet
$Case_i$	Case index
LIB	Lithium-Ion Battery
BTMS	Battery Thermal Management System
BMS	Battery Management System
EV	Electric Vehicle
HEV	Hybrid Electric Vehicle
PCM	Phase Change Material
SOC (%)	State of Charge
OCV (V)	Open-Circuit Voltage
ECM	Equivalent Circuit Model
CFD	Computational Fluid Dynamics
RANS	Reynolds-Averaged Navier–Stokes
ANSYS Fluent	CFD solver used
NRR (%)	Normalized Reduction Ratio
3C	Discharge rate (3× capacity)